

1
2
3
4
5
6
7
8
9
10
11
12
13
14
15
16
17
18
19
20
21
22
23
24
25
26
27
28

**Technical note: determination of the height of
deep-sea mooring lines above seafloor using
turbulence measurements**

by Hans van Haren

Royal Netherlands Institute for Sea Research (NIOZ), P.O. Box 59, 1790 AB Den Burg,
the Netherlands.
e-mail: hans.van.haren@nioz.nl

29 **Abstract.** Height variations $O(1)$ m of closely spaced moored oceanographic instrumentation are
30 difficult to measure in the deep sea, requiring high-accuracy pressure sensors preferably on all
31 instruments in a mooring-array. In this paper, an alternative method for relative height determination is
32 presented using 2-m spaced high-resolution temperature sensors moored on multiple 9.5-m-spaced lines
33 in the deep Western Mediterranean [Sea](#). While it was anticipated that height variations between lines
34 could be detected under near-homogeneous conditions via adiabatic lapse rate $O(10^{-4} \text{ }^\circ\text{C m}^{-1})$ by the
35 $3 \times 10^{-5} \text{ }^\circ\text{C}$ -noise-level sensors, such was prevented by the impossibility of properly correcting for short-
36 term bias due to electronic drift. Instead, a satisfactory height determination was achieved during a
37 period of relatively strong stratification and large turbulence activity. By band-pass filtering data of the
38 highest-resolved turbulent motions across the strongest temperature gradient, significant height
39 variations were detectable to within ± 0.2 m.

40

41 **1 Introduction**

42 Height variations in moored oceanographic instrumentation can occur above unknown topographic
43 features such as small rocks and gullies and, ~~e.g.~~, due to line stretching ~~by under several kN of~~ buoyancy
44 ~~force~~~~pull~~. For example, 0.005-m diameter steel cables (breaking strength ~20 kN, ~~where kN is Kilo~~
45 ~~Newton~~) stretch about 0.1% of cable length under 1.25 ~~-~~kN tension, and 0.3% under 4 ~~-~~kN tension for
46 common oceanographic (e.g., <https://www.spaceagecontrol.com/calcstre.htm>). If closely-spaced
47 mooring lines and attached instrumentation are used, one may need to correct for the unknown height
48 variations, for example to be able to distinguish thin O(1) m stratified layers. Such a correction is
49 possible using high-resolution temperature sensors.

50 In this technical-performance paper, deep-sea instrumental-height determinations will be
51 demonstrated using 45 mooring lines of 125-m tall and 9.5-m apart horizontally each holding 65 self-
52 contained high-resolution temperature ‘T-’ sensors in a 70-m diameter steel-pipe ring (van Haren et al.,
53 2021). Each line, nylon-coated 0.005-m diameter steel cable, was pulled up by a net buoyancy of 1.25
54 kN, imposed by a single buoy on top, and was attached to the anchoring ring via a suspended steel-cable
55 grid. The problem of this set-up was not so much the vertical-line stretch, but the unknown suspension
56 of the steel-cable grid. In contrast with a fixed-anchor on a single-line mooring, the steel-cable grid has
57 different heights between the anchoring steel pipes.

58 The ring was moored on a flat seafloor in nearly 2500-m deep weakly density-stratified waters of the
59 Western Mediterranean Sea. The ‘large-ring mooring’ was constructed for three-dimensional studies of
60 deep-sea internal waves, their breaking and turbulence generation, to learn more about their dynamical
61 development via short movies (van Haren et al., 2026) and detailed statistics.

62

63 **2 Materials and Methods**

64 A nearly half-cubic-hectometer of seawater was sampled using 2925 self-contained updated high-
65 resolution, stand-alone T-sensors, new version ‘NIOZ4n’. The ensemble large-ring mooring (Fig. 1a)
66 was deployed in drag-parachute controlled free-fall at the <1° flat and 2458-m deep seafloor of 42°
67 49.50’N, 006° 11.78’E of the ~~W~~~~Northw~~estern Mediterranean Sea in October 2020 (Fig. 1b). The
68 mooring was near the site of neutrino telescope KM3NeT/ORCA (Adrián-Martinez et al., 2016) off the

Field Code Changed

69 coast of Toulon, France, just 10 km south of the steep continental slope (and 5 km from its foot in the
70 abyssal plain).

71 Fig. 1c shows the numbering of 45 vertical mooring lines, which were ordered in six groups for
72 synchronisation purposes. As with all NIOZ4 T-sensors (van Haren, 2018), the individual clocks were
73 synchronised via induction to a single standard clock on the mooring-array every 4 hours, so that all T-
74 sensors were sampled within 0.01 s. Three buoys also held a Nortek AquaDopp single-point acoustic
75 current meter. Details of design, construction and deployment are given in van Haren et al. (2021).

76 With the help from Irish Marine Institute Remotely Operated underwater Vehicle (ROV) “Holland
77 I” on board Dutch R/V Pelagia, all lines with T-sensors were successfully cut and recovered in March
78 2024. Of the 45 lines, 43 were in good mechanical order, line 1.8 (line 8 of synchronization group 1;
79 henceforth indicated without decimal point) was hit by the drag parachute whereby 10 sensors were lost,
80 and line 65 was about 0.5 m lower than nominal because of a loop in the vertical line near the cable grid.
81 Only line 36 did not register synchronisation, possibly due to an electric wire failure. Three T-sensors
82 leaked and <10 were shifted in position due to tape malfunctioning. In total 2902 out of 2925 T-sensors
83 functioned as expected mechanically.

84 Due to unknown causes all T-sensors switched off unintentionally when their file-size on the 8-GB
85 Kingston memory card reached 30 MB. It implied that a maximum of 20 months of data was obtained,
86 which were recorded at an interval of once per 2 s. After post-processing, 50-150, depending on moment
87 in the record and type of analysis, extra T-sensors are not further considered due to electronics, noise
88 problems. With respect to previous NIOZ4 version, here named ‘NIOZ4o’, the slightly modified
89 electronics resulted in about twice lower noise levels of 0.00003°C and twice longer battery life.

90 Laboratory-bath calibration yielded a relative precision of <0.001°C (van Haren, 2018). Instrumental
91 electronic drift of typically 0.001°C ~~per month~~^{per month} after aging was primarily corrected by referencing
92 daily-averaged vertical profiles, which must be stable from turbulent-overturning perspective in a
93 stratified environment, to a smooth, commonly third-order, polynomial without instabilities (van Haren
94 and Gostiaux, 2012). Because vertical gradients of temperature, and thus density, are so small in the
95 deep Mediterranean so that buoyancy frequency $N = O(f)$, where f denotes the inertial frequency, a

96 secondary drift correction was applied. For this correction, reference was made to periods of typically
97 one-hour duration that were quasi-homogeneous with temperature variations smaller than instrumental
98 noise level (van Haren, 2022). Such >125-m tall quasi-homogeneous periods existed on days 350, in
99 2020, 453 and 657, both -366 in 2021, in the records. These two drift corrections allowed for proper
100 calculations of turbulence values using the method of Thorpe (1977), as extensively described for
101 moored T-sensors in van Haren and Gostiaux (2012) and van Haren (2018), under weakly stratified
102 conditions. As will be demonstrated in Appendix A, under very weakly stratified conditions with $N <$
103 $0.5f$ a tertiary drift correction involved low-pass filtering of data. This additional correction addresses
104 short-term drift that was about 2-3 times larger in NIOZn than in NIOZo T-sensors.

105

106 **3 Results**

107 While a single-line mooring attached to an anchor at the seafloor may modify the nominal positions of
108 instrumentation due to buoyancy-stretch of typically 0.1-1% of the total line length, depending on
109 amount of buoyancy and line fabric and make, the large-ring mooring will experience an additional
110 differential positioning due to the variable anchor height of the cable grid. Given the anchor being the
111 steel ring, the distributed buoys on top of each of the 45 lines are expected to pull the steel-cable grid
112 (Fig. 1) up in the form of a dome. Hence, different heights are expected for different lines above the,
113 presumed flat, seafloor. Simple geometrical models mimicking a dome will be compared with
114 observations of height variations between the different mooring lines.

115 Prior to deployment, stretch-tests were performed with the grid's steel cable on a harbour quay.
116 Under nominal tension of the planned buoyancy it was found that the exerted tension delivered a
117 measured cable stretch to a value that the typical angle of grid inflection was expected to amount 5° .
118 This angle to the horizontal could not be verified from visual inspection using ROV, although at various
119 images a non-zero angle is discernible, which also seems to vary between different cable sections in the
120 grid (Fig. 2a), as, e.g., in a dome.

121 Eight 'corner-lines' (Fig. 1c, 2b) were also displaced to an amount not precisely verifiable from
122 ROV-inspection. These lines were attached differently to the steel-cable grid as they could not be
123 attached directly to their intersection points at the steel ring. Estimating the height of corner-line can be

124 attempted from Fig. 2b. Visually, the right side of the small ring holding a vertical line in its center does
125 not touch seafloor and the small ring rotates around the smallest of three short assist cables of which the
126 centre is elevated to approximately $h = 0.6$ m above seafloor. If angles are measured on the basis of
127 vertical/horizontal ratio 4/4.5, then the small-ring makes an angle of about 40° to the horizontal, so that
128 its center is 0.8 m above the edge of the small-ring. In that case, the corner-line will start at $h = 1.0$ m.

129

130 **3.1 Parabola model**

131 Taking the 5° -angle due to distributed tension stretch as starting point, some simple models of half cable-
132 grid cross-section can be made (Fig. 3). Quasi-parabola and straight-cable models are considered.
133 Considering that grid attachments are made in the center of the large-ring pipes at 0.3 m, the models
134 start from that height above seafloor. All grid attachments were made to extra enforced steel rings that
135 were bolted around the pipes, to guarantee the pipes remain circular. The steel rings and pipes were
136 protected against corrosion with zinc anodes (Fig. 2).

137 The simplest, albeit unrealistic, straight-cable model makes a fixed angle of 5° (green model in Fig,
138 3). A slightly better model is a paraboloid, a 3D form of the mathematical parabola, as would be
139 approximately found in a weighed cable grid held upside down under gravity. A 5-m discretized
140 parabola model intersecting the straight-cable model halfway will have its top at $h = 2.07$ m above (blue
141 model). The steepest part, exceeding 5° , of the cable in this model has a horizontal distance of 5 m to
142 the large ring, which corresponds with the position of, e.g., line 57 (cf. Fig. 1c). In the model, line 57
143 has its lowest T-sensor at $h = 1.2$ m. If an overall maximum angle of 5° is maintained, the top of that
144 parabola model will be at $h = 1.12$ m, and the first line inside the large ring will have its lowest T-sensor
145 at $h = 0.72$ m (red model). In an attempt to verify these cable-grid models, data from the altimeter and,
146 in a relative sense, the pressure gauge of the ROV were used. They gave a value of $h = 0.7 \pm 0.1$ m after
147 the ROV had landed on the small-ring of the first line of the grid's centre cable.

148 If the maximum- 5° parabola model is correct, all vertical lines are a maximum of 0.4 m, or ± 0.2 m,
149 apart vertically. This is difficult to correct for in practice. Unfortunately no pressure sensors were
150 available on the vertical lines, the three mounted on current meters being too inaccurate, to quantify

151 height variations between lines. As a result, quantification is sought using the T-sensor data to verify,
152 and possibly improve when necessary, above geometrical model values.

153

154 **3.2 Adiabatic lapse rate height-determination method**

155 Considering that the T-sensors have a noise level of 0.00003°C, potential temperature differences of
156 $>5 \times 10^{-5}$ °C are statistically significantly detectable, in theory. Thus, given local deep Western
157 Mediterranean adiabatic lapse rate of $\Gamma = -1.7 \times 10^{-4}$ °C m⁻¹ (here for simplicity a pressure of 10⁴ Pa is
158 transferred to a vertical distance of 1 m), vertical height differences of >0.3 m are potentially detectable
159 using T-sensor data under near-homogeneous conditions in which temperature variations are
160 predominantly due to compressibility effects. Such conditions do occur in the deep Western
161 Mediterranean regularly, see the lower 250 m above seafloor in a shipborne-CTD profile (Fig. 4). Γ
162 dominates the temperature lapse with the vertical in Fig. 4a. In time series from moored T-sensor data,
163 near-homogeneous conditions over 125-m vertical range occur about 60% of the time (Fig. 5a). These
164 conditions lead to very low temperature variance across all frequencies outside instrumental white noise
165 (Appendix A).

166 However, a complicating factor in ‘adiabatic lapse rate height-determination’ method is the
167 electronic drift of T-sensors, which varies in intensity per sensor but typically amounts about 10^{-3} °C
168 ~~per month~~^{mo⁻¹}. While the value is one order of magnitude larger than the adiabatic lapse rate per unit
169 length, in principle T-sensors attached to a particular vertical line can be corrected to within a precision,
170 i.e. relative accuracy, of 10^{-4} °C (van Haren, 2018). All depends on a calibration with a precision of
171 $<5 \times 10^{-4}$ °C, which is achievable using a thermostatic bath with constant temperature levels to within
172 $\pm 10^{-4}$ °C of their preset values. The standard post-processing correction is by fitting a smooth curve over
173 sufficiently time-averaged vertical temperature profile that must be stable over an inertial period. When
174 the temperature range is not too large, above precision is obtainable with some effort and careful search
175 in the data. In the weakly stratified deep Mediterranean however, this correction is not achievable
176 between different lines, because the low precision is not transferrable to a low absolute accuracy.

177 As a result, the height determinations from translated temperature differences between lines attached
178 to the steel-cable grid are too large and erratically distributed (Fig. 6). Obviously, there is no consistency
179 between lines in the image of Fig. 6, which shows no signs of expected lower relative values at the edges
180 close to the ring and higher values near the center, following parabola models as in Fig. 3. Moreover,
181 the variation in values is nearly an order of magnitude greater than expected from the parabola models
182 in Fig. 3. Clustering per calibration -- approximately 190 T-sensors are used in the thermostatic bath per
183 cycle (van Haren, 2018) -- does not give improvement of consistency in the image (not shown).

184

185 3.3 Turbulence variance height-determination method

186 As the adiabatic pressure effect on temperature is not a suitable measuring method for the expected
187 doming of the steel-cable grid inside the large ring, another method is sought. In contrast with the
188 adiabatic lapse rate method, this other method is not working under near-homogeneous conditions.
189 Instead, it works when vertical temperature stratification is rather large, with peaks resulting in $N = 6f$,
190 and turbulent temperature variations are large (Figs 5a, 7, 8). The combination of these two conditions,
191 relatively large stratification and large turbulence, seems counter-intuitive, as stratification is generally
192 considered to suppress turbulence. Whilst stratification indeed suppresses the vertical length-scale of
193 turbulence, it may have variable effects on temperature variance.

194 In case of the deep Western Mediterranean, relatively large vertical temperature gradients of a few
195 10^{-3} °C over O(10-100) m occur with the advection of warmer waters (Figs 5a, 7a). The advection is
196 regularly slanted towards the vertical, either induced by internal-wave action and/or by sub-mesoscale
197 and mesoscale eddies, as inferred from quasi-3D movies (van Haren et al., 2026). When mainly
198 governed by planetary vorticity deflection, it represents in part convection-turbulence that appears in a
199 vertically stratified environment at mid-latitudes (Marshall and Schott, 1999). All warming events
200 observed thus far associate with considerable turbulence. In the entire time series (Fig. 5a) no significant
201 cooling events occur. Current speeds (Fig. 5b) seldom exceed 0.1 m s^{-1} and thus ~~there is no~~
202 evidence strong flow events such as associated with deep dense-water formation that might occur in late
203 winter, ~~but is not observed.~~

204 Due to the relatively low-noise T-sensors, deep Western-Mediterranean waters can be characterized
205 by frequency (ω) spectra in which turbulence manifests itself over a range of at least two orders of
206 magnitude (Fig. 8), approximately across $10 < \omega < 3000$ cpd (cycles per day), under the relatively large
207 turbulence conditions. Outside this band, spectra are dominated by internal waves, for $\omega < 10$ cpd, and
208 roll-off to instrumental white noise, for $\omega > 3000$ cpd. A strong temperature gradient produces high-
209 frequency internal waves, but is also accompanied by turbulent eddies, probably as a result of breaking
210 internal waves. Under near-homogeneous conditions similar temperature spectra are found, except that
211 the variance is two orders of magnitude lower and turbulence drops into instrumental noise at about 500
212 cpd (*cf.* Fig. A2).

213 Here, we take the high-frequency portion $\Theta'(t, z)$ of the well-resolved turbulence band and, somewhat
214 arbitrarily, band-pass filter between $600 < \omega < 1800$ cpd (frequency range indicated by the black bar in
215 Fig. 8) that is certainly outside internal wave and white noise bands. Although temperature variations in
216 this range are part of inertial subrange of isotropic turbulence (Kolmogorov, 1941) reflecting a continual
217 transfer between large energy-containing turbulence scales and small dissipative scales via shear-
218 induced motions, such are mainly found well away from the seafloor. Within $h = O(10)$ m from the
219 seafloor, motions are partly of isotropic nature and partly of anisotropic convection-turbulence nature
220 in a buoyancy subrange (Bolgiano, 1959; Obukhov, 1959), which manifests at all heights in the range
221 $10 < \omega < 100$ cpd, albeit the spectral smoothing is coarse. Irrespective of a variation in slope and
222 turbulence behaviour, the main goal here is the practical use of temperature (turbulence) variance
223 outlined below. Future investigations will be directed to improve statistics in part by averaging data
224 from the 45 lines and data from different periods of stratified turbulence.

225 During such a period of slanted warm waters from above, temperature variance may be relatively
226 low within a few meters from the seafloor, but it increases to high levels well above common interior-
227 values in $O(10)$ m above seafloor (Figs 8, 9). The 1.3-day root-mean-square value of the 600-1800 cpd
228 band-pass filtered signals is calculated for every T-sensor. In this example, the peak in turbulence-
229 temperature variance is found around $h = 11$ m. Above and below the peak one can take advantage of
230 two depth-levels of high gradients in turbulence temperature-variance. Common interior-values are

231 reached at about $h > 40 \text{ m} = h_{\text{sst}}$, which could reflect the upper limit of layer of strong stratified turbulence
232 ~~'sst'~~ (Figs 7-9).

233 After ~~referencing~~ local turbulence temperature variance- $\Theta'^2(\text{line}, z)$ - ~~to the value of an~~
234 ~~arbitrary line(x), by subtracting $\Theta'^2(\text{line}(x), z)$, taking the mean of two levels z1 and z2 and scaling~~ with
235 the 45-line average $\langle \cdot \rangle$ value of ~~their~~ vertical gradient $\langle d\langle \Theta'^2 \rangle / dz \rangle$ over $dz = \underline{2\text{-m}}$, ~~commonly~~
236 the, here constant, 2-m distance between T-sensors, a transfer from temperature to height value is
237 established. Hereby it is assumed that over the 1.3-day period the statistics are homogeneous over the
238 mooring array. Heterogeneity is not expected to affect the average value over a period longer than the
239 inertial period. Subsequently, below or above the peak value in Fig. 9, a height pattern can be computed
240 relative to values of an arbitrary vertical line, 44 in this case (Fig. 10). Here, the pattern is given for
241 height determination by computing across the largest gradient of temperature-variance, between T-
242 sensors at $h = 3.5$ and 5.5 m. An example of an eight times shorter period is given in Appendix B.

243 The difference between this pattern and that in Fig. 6 is obvious. First, all values are between 0 and
244 2 m in Fig. 10, and a consistent statistical significance is found to within ± 0.2 m. Cross-sections of the
245 cable grid also confirm the doming of the pattern (Fig. 11). While the observed doming is close to the
246 parabola models of Fig. 3, larger height-determination values than in the models are observed in the
247 center, with slightly steeper overall grid cables that still roughly obey the maximum 5° slopes (Fig. 11).
248 The $\pm 0.2\text{-m}$ error range is easily verifiable after comparison with the provided bar. Corrections to
249 vertical positioning of T-sensors are therefore feasible and necessary, because the difference between
250 the center and edges of the cable grid is approximately 1.5 m.

251

252 3.4 Stratified turbulence quantification

253 The temperature variations of the well-stratified day 485 demonstrating the necessary height
254 determination for the doming of the steel-cable grid show a background value of turbulence dissipation
255 rate $O(10^{-10}) \text{ m}^2 \text{ s}^{-3}$. Reduced values $O(10^{-11}) \text{ m}^2 \text{ s}^{-3}$ are basically only found within a few meters from
256 the seafloor, underneath the largest 2-m small-scale stratification with maximum buoyancy-frequency
257 values of $N_{\text{max}} \approx 1.6 \times 10^{-3} \text{ s}^{-1}$ (Fig. 7). This is observable in time-depth plots of temperature, small-scale

258 stratification and non-averaged turbulence dissipation rate 'values'. The largest overturns, which
259 dominate the vertically averaged values of turbulence dissipation rate, have a scale $O(100)$ m (Fig. 7a,c).
260 Turbulent overturns reach close to the seafloor, but only sporadically touch it, mostly at begin and end
261 of the warm-water depression. Coarsely every two hours, 124-m vertically averaged turbulence
262 dissipation rate peaks in value (Fig. 2d). The $h = 40$ m of elevated high-frequency temperature variance
263 (Fig. 9) and stratification (Fig. 7b) show non-negligible turbulence dissipation rate values with further
264 elevated values reaching the seafloor before and after the warm-water passage (Fig. 7c).

265 Time-depth mean values from the 1.3-day period are for turbulence dissipation rate $[\langle \varepsilon \rangle] = 6 \pm 3 \times 10^{-10}$
266 m^2s^{-3} and for turbulent diffusivity $[\langle K_z \rangle] = 1.4 \pm 0.7 \times 10^{-3} \text{m}^2\text{s}^{-1}$ under $[\langle N \rangle] = 2.8 \pm 0.3 \times 10^{-4} \text{s}^{-1} \approx 3f$.
267 These 1.3-day, 124-m mean turbulence values are about one order of magnitude larger than open-ocean
268 values observed in stratified waters well away from boundaries (Gregg 1989; de Lavergne et al. 2020;
269 Yasuda et al. 2021). The reader is reminded that the experiment was located close to the foot of the
270 continental slope, where the strong Liguro-Provençal current flows, (internal) tides are weak, and total,
271 (sub-)mesoscale plus near-inertial, water-flow speeds never exceed 0.1m s^{-1} .

272 Although the warm-water event of Fig. 7 is of relatively strong turbulence, it is not exceptional and
273 elevated temperature-stratification and -variance alternate in time with near-homogeneous episodes
274 throughout the 20-month records (Fig. 5a). This will be reported elsewhere in more detail, notably using
275 three-dimensional investigations.

276

277 **4 Conclusions**

278 The expected height variation due to vertical buoyancy pull across a steel-cable grid, which was
279 suspended within a large anchoring steel-pipe ring, was modelled as an inverted parabolic with
280 maximum 5° angle to the horizontal. To verify the height variation of the instrumented vertical mooring
281 lines across the grid, we expected to use an observational period with negligibly small vertical density,
282 and thus temperature, stratification so that the adiabatic lapse rate $\Gamma = dT/dz$ would dominate vertical
283 temperature variations $T(z)$. The T-sensors have a noise level of about $3 \times 10^{-5} \text{ }^\circ\text{C}$, while $|\Gamma| \approx 1.7 \times 10^{-4}$
284 $^\circ\text{C m}^{-1}$ in the deep Western Mediterranean and thus is potentially measurable by sensors nominally 2-m

285 apart vertically. However, the sensor’s electronic drift at all scales turned out insufficiently correctable
286 under near-homogeneous conditions.

287 Instead, a mooring-height determination was achieved during a period of relatively large
288 stratification, during a slump down of warm water presumably slanted from above and induced by
289 internal waves. By band-pass filtering the highest resolved turbulence variance, mainly from inertial
290 subrange, across the strongest temperature gradient, the dome of pulled-up grid was significantly
291 detectable, and fine-tuned a parabola model with height variations between the moorings of correctable
292 $(0.5-2.0)\pm 0.2$ m.

293 The impact of investigating turbulence signals from high-resolution moored T-sensors in the deep
294 Mediterranean is several-fold. First, it demonstrates the dynamics of internal-wave breaking governed
295 by either near-inertial or sub-mesoscale motions slumping relatively warm waters to within a few meters
296 above the seafloor. Thereby, an episodic-average turbulence dissipation rate is provided, which is about
297 ten times larger than ambient values above a flat seafloor. The enhanced turbulence affects deep-sea
298 life. Deep-sea turbulence is studied more elaborately in van Haren (2026 submitted).

299 Second, the strong vertical variation in turbulence temperature-variance profiles, across relatively
300 large local vertical temperature gradients, may be useful for height determinations in nearby moorings
301 over flat seafloors also in shallow seas, and, more difficult, above sloping seafloors, whereby a
302 correction may be applied for unknown mooring-line stretch under tensioning by buoyancy. Such height
303 determinations may also be necessary when moorings are accidentally placed on small rocks or in small
304 gullies. The resulting determination demonstrated that the parabola model based on in-house line-
305 tensioning was adequate and required only secondary adjustment in the slightly steeper cables of the
306 underwater large-ring mooring, albeit all showed $<5^\circ$ sloping to the horizontal as anticipated from the
307 in-house tests.

308

309 *Data availability.*

310 Processed temperature data used in this study are available from van Haren (2026) “Processed
311 temperature data to: Determination of the height of deep-sea mooring lines above seafloor using
312 turbulence measurements”. Mendeley Data, V 1. <https://doi.org/10.17632/24n7dwjhp1.1jphwzjhg1>.

Formatted: English (United States)

Field Code Changed

Formatted: Hyperlink, English (United Kingdom)

313 ~~Only raw data are stored from the T sensor mooring array. Analyses proceed via extensive post~~
314 ~~processing, including manual checks, which are adapted to each specific analysis task. Because of the~~
315 ~~complex processing the raw data from the custom made T sensors are not made publicly accessible.~~

316 Current meter and CTD data are available from van Haren (2025): “Large-ring mooring current meter
317 and CTD data”, Mendeley Data, V1, <https://doi.org/10.17632/f8kfwcvtdn.1>.

318

319 *Competing interests.* The author has no competing interests.

320

321 *Acknowledgments.* This research was supported in part by NWO, the Netherlands organization for the
322 advancement of science. Captains and crews of R/V Pelagia are thanked for the very pleasant
323 cooperation. The team of ROV Holland I performed an excellent underwater mission to recover the
324 instrumentation of the large ring. NIOZ colleagues notably from the NMF department are especially
325 thanked for their indispensable contributions during the long preparatory and construction phases to
326 make this unique sea-operation successful. I am indebted to colleagues in the KM3NeT Collaboration,
327 who demonstrated unison to get large-scale infrastructural projects funded. M. de Jong and A. Heijboer
328 helped in securing NWO funding.

329

330 **Appendix A Extra drift correction for T-sensors in near-homogeneous waters**

331 When waters are very weakly stratified or near-homogeneous with $N < 0.5f$ over the range of moored
332 T-sensors, a short-term drift error may emerge. This drift partially causes the impossibility to determine
333 instrumental height variations under such conditions. Albeit electronic drift is well known to occur on
334 long timescales of weeks-months, short-term hourly drift may appear because of nonlinear temperature
335 dependency and/or inadequate contact between the Negative Temperature Coefficient NTC thermistors
336 and the environment through the glass tube and its contact paste. NTC thermistors are the measuring
337 component of NIOZ T-sensors. This short-term drift was previously observed in NIOZ4o deep-trench
338 data and, especially clear, in air (van Haren and Bosveld, 2022). It turned out difficult to correct for.
339 During a 2017/2018 test experiment in the deep Western Mediterranean it did not pose a great problem
340 in NIOZ4o data. Unfortunately, NIOZ4n appear to have about twice larger short-term drift than previous
341 NIOZ4o, despite their smaller long-term drift and smaller instrumental noise, both by a factor of two-
342 three approximately. A correction for short-term drift of NIOZ4n is proposed below, with reference to
343 NIOZ4o.

344 Half-day NIOZ4n data (Fig. A1a-c) from arbitrary line 25 are compared with a 104-m tall set of
345 NIOZ4o data (Fig. A1d-f). The investigated samples are from almost homogeneous waters, with a total
346 colour-range over a Conservative-Temperature difference of only 1.7×10^{-4} °C, for both data sets.
347 Although NIOZ4o are more noisy (Fig. A1a,d), the NIOZ4n show a more horizontal-stripy pattern that
348 has different values through time, compared to T-sensors above and below. This is evidence of
349 remaining bias due to short-term drift. Low-pass time filtering, with a cut-off frequency of 500 cpd,
350 does not reduce these (Fig. A1b,e), but additional vertical filtering, with a cut-off wavenumber at 10
351 cpm, adequately removes the bias (Fig. A1c,f).

352 As a consequence of near-homogeneity, energetic overturning scales are expected to be large due to
353 the reduced restoring force. In both data sets in the center of images, albeit clearer in the NIOZ4o, one
354 notices a slanting jet of warmer waters over a vertical range of about 60 m in short bursts of 10-20 m.
355 Such jets of convection turbulence were found abundant in the Mariana Trench (van Haren, 2023), but
356 relatively rarely in the deep Mediterranean.

357 Depending on the rate of stratification, the vertical filter cut-off at 0.05-0.2 cpm (cycles per meter)
358 is obtained after fine-tuning in an attempt to retain the relevant overturning scales as much as possible.
359 Under weakly but stable stratified conditions 0.1-0.2 cpm is used, while under near-homogeneous and
360 unstable conditions 0.05-0.1 cpm is used. The fine-tuning of the vertical filter concerns relatively
361 adequate spectral improvement and turbulence calculations. Naturally, all data-corrections yield a
362 certain loss of information, but it is informative to estimate how much the loss may be.

363 In 4-d-average spectra (Fig. A2) that include the 0.5-d period of Fig. A1, the impact of small-scale
364 drift is seen to be larger for NIOZ4n (Fig. A2a) than for NIOZ4o (Fig. A2b). In these plots spectra are
365 scaled with the slope of buoyancy subrange, for clarity. As a reference for the correction, the temperature
366 difference $\Delta\Theta$ (magenta spectrum) is taken between the two neighbouring T-sensors at $h = 29$ and 31
367 m. That difference spectrum is compared with the spectrum of temperature data from the upper T-sensor
368 (green). The magenta spectrum has a higher noise level by about a factor of two for $\omega > 100$ cpd than
369 that of the green spectrum. This is commensurate with random white noise.

370 At lower frequencies, the magenta spectrum crosses the green spectrum around 50 and 150 cpd for
371 Fig. A2a and A2b, respectively. This means that data are no longer dominated by white noise, but by
372 other parametrizations, which are governed either by natural processes or by instrumental flaws other
373 than noise. Around the crossing frequency, temperature spectra become horizontal following buoyancy-
374 subrange scaling. This scaling, which represents convection turbulence of an active scalar (Bolgiano,
375 1959; Obukhov, 1959), was no longer dominant at frequencies higher than that of the crossing, more so
376 in Fig. A2b than in Fig. A2a.

377 After correction by applying vertical low-pass-filtering (red), the weak slope towards lower
378 frequencies, especially that of Fig. A2a, is correctly removed and white noise levels are lower. The
379 spectral slope change to white noise is now at the same frequency, 400 cpd, for both data sets. The quasi-
380 transfer function of correction depicted in the blue spectra is less steeply sloping for $\omega < 1000$ cpd in
381 Fig. A2a than in Fig. A2b, which demonstrates the larger effects of short-term drift correction for the
382 NIOZ4n compared to the NIOZ4o. However, in both data sets of very weakly stratified deep-sea waters

383 it prevents resolution of the transition from buoyancy and/or inertial subranges to the viscous turbulence
384 dissipation range.

385 Resuming, after vertical-filtering correction, temperature data at $\omega < 400$ cpd seem useful for
386 turbulence calculations under weakly stratified conditions. Note that this correction is not needed during
387 periods with relatively large temperature variance and stratified, generally more shear-induced,
388 turbulence. For turbulence dissipation rate calculations, 10-30% reduction is obtained from short-term
389 drift correction. This reduction is well within the error range of a factor of two normally achieved for
390 ocean turbulence data.

391

392 **Appendix B Height determination from a short warm-water period**

393 Naturally the method sketched in Section 3.3 does not work under all circumstances. One requires a
394 rather vigorous appearance of stratified warm-water turbulence to preferably reach close to the seafloor.
395 Such periods are sought manually. Even a short 3.6-h period returns a reasonable estimate of the cable
396 grid height (Fig. A3). It mimics Fig. 10, and has some larger noise level with values that remain within
397 the error bar.

398

399 **References**

- 400 Adrián-Martínez, S., Ageron, M., Aharonian, F., Aiello, S., Albert, A., et al.: Letter of intent for
401 KM3NeT 2.0, *J. Phys. G*, 43, 084001, 2016. DOI 10.1088/0954-3899/43/8/084001
- 402 Bolgiano, R.: Turbulent spectra in a stably stratified atmosphere, *J. Geophys. Res.* 64, 2226-2229, 1959.
403 <https://doi.org/10.1029/JZ064i012p02226>
- 404 de Lavergne, C., Vic, C., Madec, G., Roquet, F., Waterhouse, A. F., and Whalen, C. B. et al.: A
405 parameterization of local and remote tidal mixing, *J. Adv. Mod. Earth Sys.*, 12,
406 e2020MS002065, 2020. <https://doi.org/10.1029/2020MS002065>
- 407 Gregg, M. C.: Scaling turbulent dissipation in the thermocline, *J. Geophys. Res.*, 94, 9686-9698, 1989.
408 <https://doi.org/10.1029/JC094iC07p09686>
- 409 IOC, SCOR, and IAPSO: The International Thermodynamic Equation of Seawater – 2010: Calculation
410 and Use of Thermodynamic Properties, Intergovernmental Oceanographic Commission,
411 Manuals and Guides No. 56, UNESCO, Paris (F), 196 pp, 2010.
412 <https://unesdoc.unesco.org/ark:/48223/pf0000188170>
- 413 Kolmogorov, A. N.: The local structure of turbulence in incompressible viscous fluid for very large
414 Reynolds numbers, *Dokl. Akad. Nauk SSSR*, 30, 301-305, 1941.
- 415 Marshall, J., and Schott, F.: Open-ocean convection: Observations, theory, and models, *Rev. Geophys.*,
416 37, 1-64, 1999. <https://doi.org/10.1029/98RG02739>
- 417 Obukhov, A. M.: Effect of buoyancy forces on the structure of temperature field in a turbulent flow,
418 *Dokl. Akad. Nauk SSSR*, 125, 1246-1248, 1959.
- 419 Thorpe, S. A.: Turbulence and mixing in a Scottish loch, *Phil. Trans. Roy. Soc. Lond. A*, 286, 125-181,
420 1977. <https://doi.org/10.1098/rsta.1977.0112>
- 421 van Haren, H.: Philosophy and application of high-resolution temperature sensors for stratified waters,
422 *Sensors*, 18, 3184, doi:10.3390/s18103184, 2018. <https://doi.org/10.3390/s18103184>
- 423 van Haren, H.: Thermistor string corrections in data from very weakly stratified deep-ocean waters,
424 *Deep-Sea Res. I*, 189, 103870, 2022. <https://doi.org/10.1016/j.dsr.2022.103870>
- 425 van Haren, H.: How and what turbulent are deep Mariana Trench waters? *Dyn. Atmos. Oc.*, 103, 101372,
426 2023. <https://doi.org/10.1016/j.dynatmoce.2023.101372>

427 van Haren, H., and Bosveld, F. C.: Internal wave and turbulence observations with very high-resolution
428 temperature sensors along the Cabauw mast, *J. Atmos. Ocean. Technol.*, 39, 1149-1165, 2022.
429 <https://doi.org/10.1175/JTECH-D-21-0153.1>

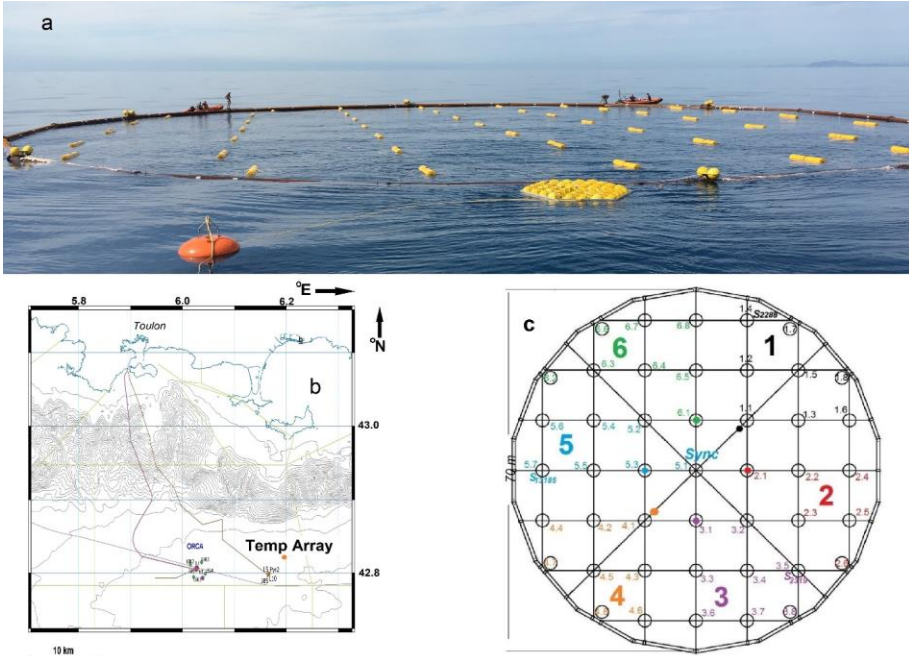
430 van Haren, H. and Gostiaux, L.: Detailed internal wave mixing observed above a deep-ocean slope, *J.*
431 *Mar. Res.*, 70, 173-197, 2012.
432 https://elischolar.library.yale.edu/journal_of_marine_research/337

433 van Haren, H., Bakker, R., Witte, Y., Laan, M., and van Heerwaarden, J.: Half a cubic hectometer
434 mooring-array 3D-T of 3000 temperature sensors in the deep sea, *J. Atmos. Ocean. Technol.*,
435 38, 1585-1597, 2021. <https://doi.org/10.1175/JTECH-D-21-0045.1>

436 van Haren, H., Adriani, O., Albert, A., Alhebsi, A. R., Alshalloudi, S., et al.: Whipped and mixed warm
437 clouds in the deep sea, *Geophys. Res. Lett.*, 53, e2025GL119998, 2026.
438 <https://doi.org/10.1029/2025GL119998>

439 Yasuda, I., Fujio, S., Yanagimoto, D., Lee, K.J., Sasaki, Y., et al.: Estimate of turbulent energy
440 dissipation rate using free-fall and CTD-attached fast-response thermistors in weak ocean
441 turbulence, *J. Oceanogr.*, 77, 17-28, 2021. <https://doi.org/10.1007/s10872-020-00574-2>

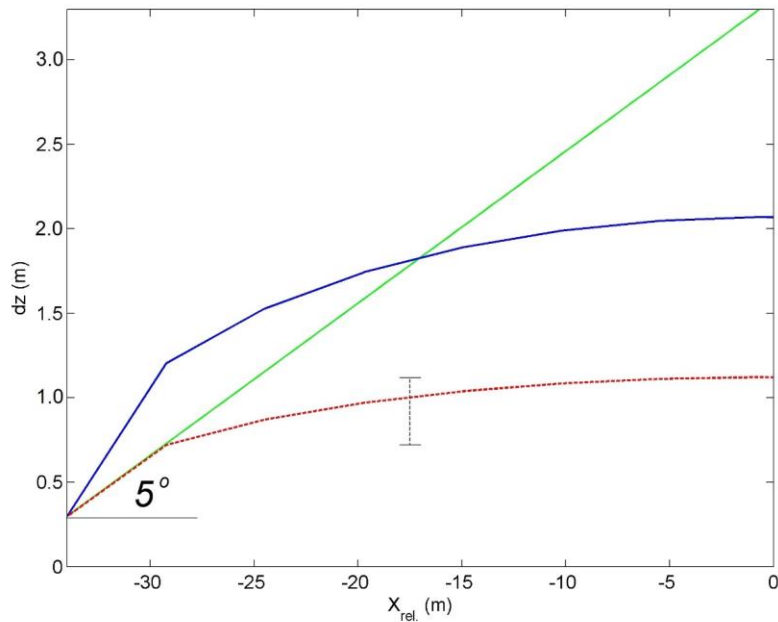
442



443
 444 **Figure 1.** Large ring in fold-up form at sea, during deployment just prior to finish the opening of air-
 445 valves. The front part of the large steel-pipe ring is already underwater. Almost all top-buoys of the 45
 446 small-ring-compacted mooring lines are visible. In the front still outside the ring, the yellow drag
 447 parachute and orange pick-up buoy are floating. (b) Location named "Temp Array" (orange dot) off
 448 southern France. The mooring is well east of main neutrino telescope 'NT' site "ORCA" of KM3NeT
 449 (Adrián-Martinez et al., 2016) and just northeast of the former ANTARES NT-site. Isobaths are given
 450 every 100 m. (c) Layout of the large-ring mooring viewed from above, with steel-cable grid and small-
 451 rings numbered in six synchronisation groups. Lines 14, 35 and 57 (omitting the decimal point) held a
 452 current meter at the top-buoy. Corner-lies are, in clockwise direction: 17, 18, 26, 38, 48, 47, 62 and 66.
 453

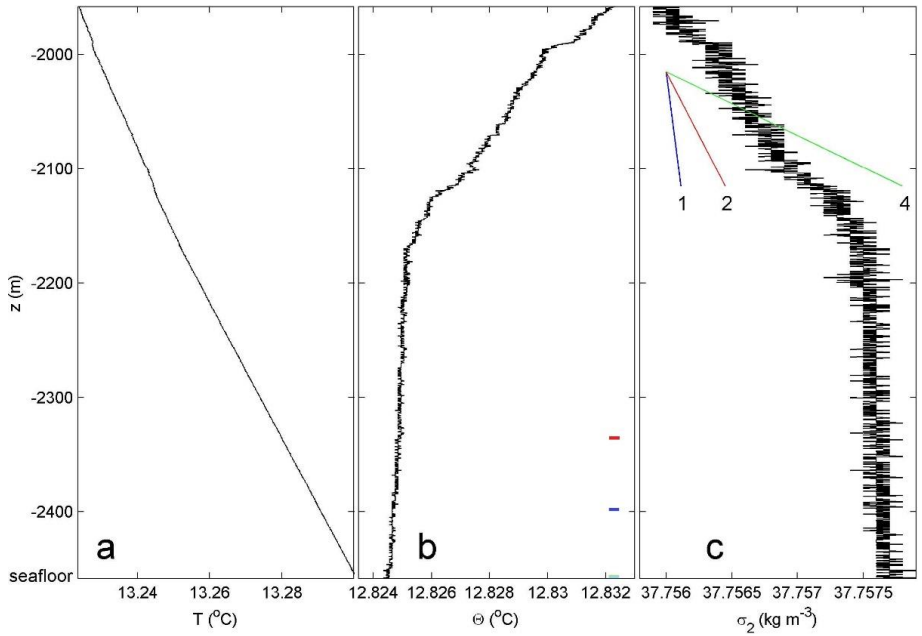


454
 455 **Figure 2.** Underwater video stills of small-rings demonstrating steel-cable grid elevation and cable-
 456 inclinations. The 0.61-m diameter steel pipe in the foreground is part of the large anchoring ring, which
 457 sank 0.07 ± 0.02 m in the sediment of the $< 1^\circ$ flat seafloor. All steel cables are attached to the middle of
 458 the steel pipes, and thus at height $h = 0.24$ m above sediment. (a) Line 44 (cf. Fig. 1c). To the right of
 459 the small-ring the wire visibly makes a larger angle to the horizontal than to the left. (b) Estimating
 460 height of ‘corner-line’ 47, see text. (Images from video by ROV Holland I).
 461

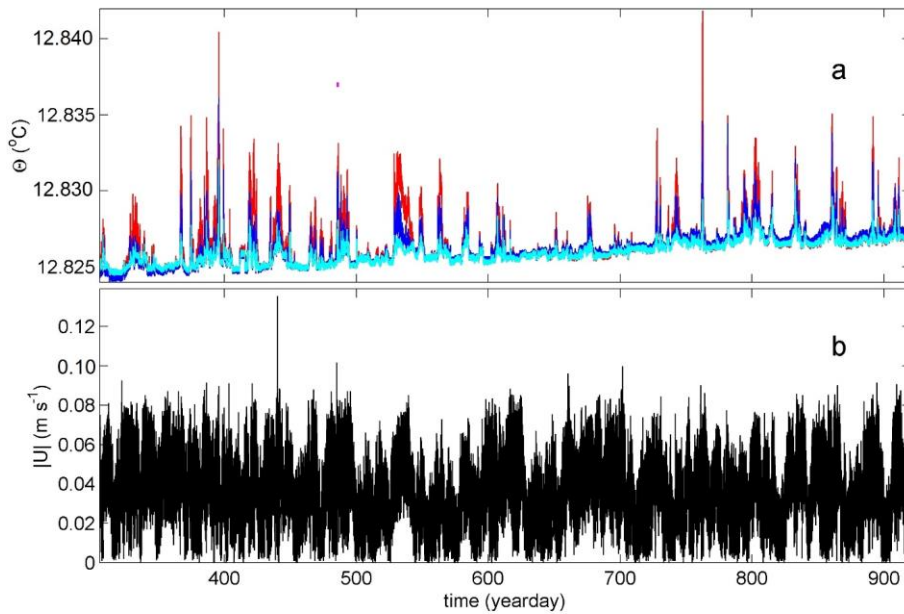


462
 463 **Figure 3.** Some expected quasi-parabola and straight-line models, for half centre steel cable of large-
 464 ring mooring grid. The seafloor is at the horizontal axis, the cable-grid attachment to the large-ring is
 465 for a steel pipe at a solid floor. The green straight line has a fixed angle of 5° with the horizontal, which
 466 angle was established after in-port tension tests. The blue (solid line, 5-m discretized) parabola model
 467 intersects the green line halfway, so that its top is at $h = 2.07$ m. If an overall maximum angle of 5° is
 468 maintained (red dashed model), the parabola top is at $h = 1.12$ m, and the first vertical line attached to
 469 relative horizontal position $x_{rel} = -29$ m will be at $h = 0.72$ m.

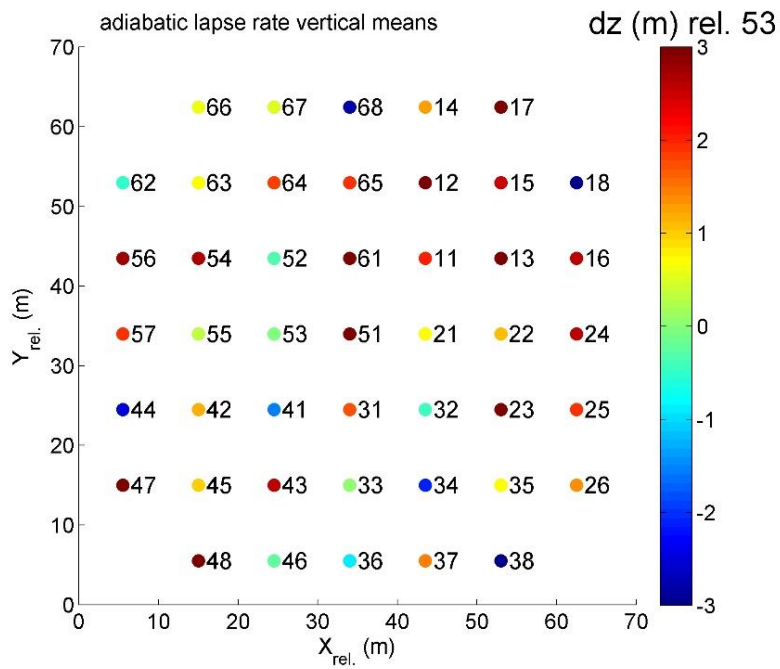
470



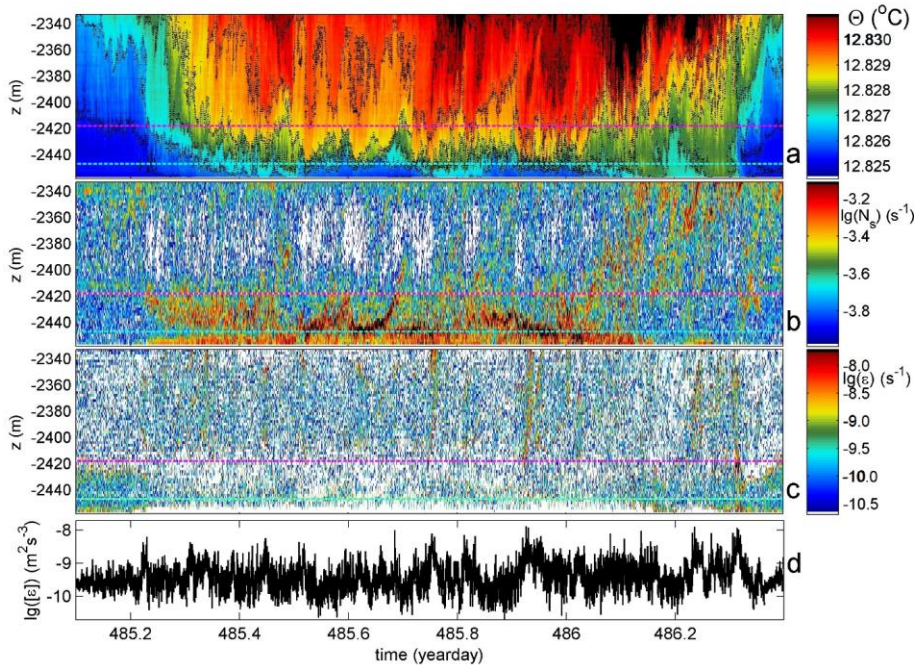
471
 472 **Figure 4.** Lower 500 m of shipborne CTD-profile data obtained near the large ring during mooring
 473 deployment. (a) In situ temperature. (b) Conservative Temperature (IOC et al., 2010), data in a. corrected
 474 for compression. Small colour bars indicate nominal heights of moored T-sensors at lowest (cyan),
 475 middle (blue) and upper (red) positions. (c) Density anomaly referenced to 2×10^7 Pa. The sloping lines
 476 indicate several stratification rates in terms of buoyancy frequency $N = xf$, $x = 1, 2, 4$ times the local
 477 inertial frequency f .
 478



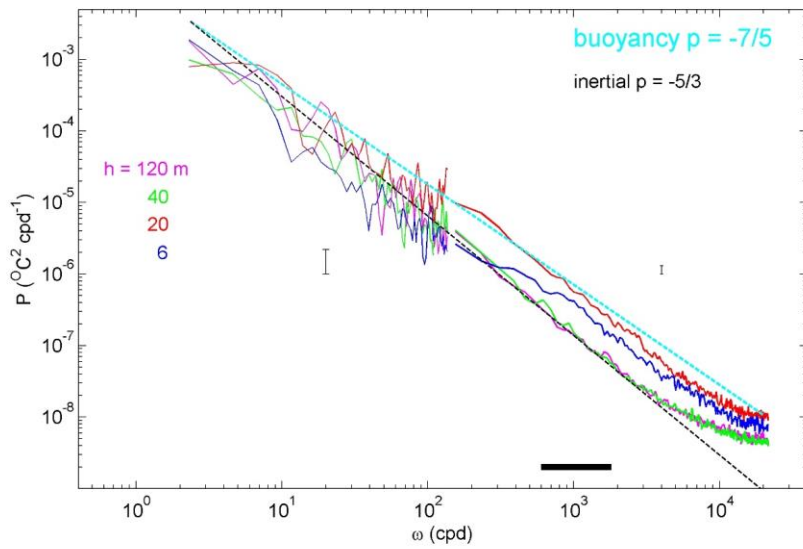
479
 480 **Figure 5.** Overall 20-month time series of moored temperature and current meter data. (a) Conservative
 481 Temperature at $h = 1$ (cyan), 63 (blue) and 125 m (red) cf. Fig. 4b of arbitrary line 53. Data are
 482 subsampled at once per 6 s and not corrected for electronic-drift bias. The magenta dot indicates day
 483 485. (b) Unfiltered current speed at $h = 126$ m of line 14.
 484



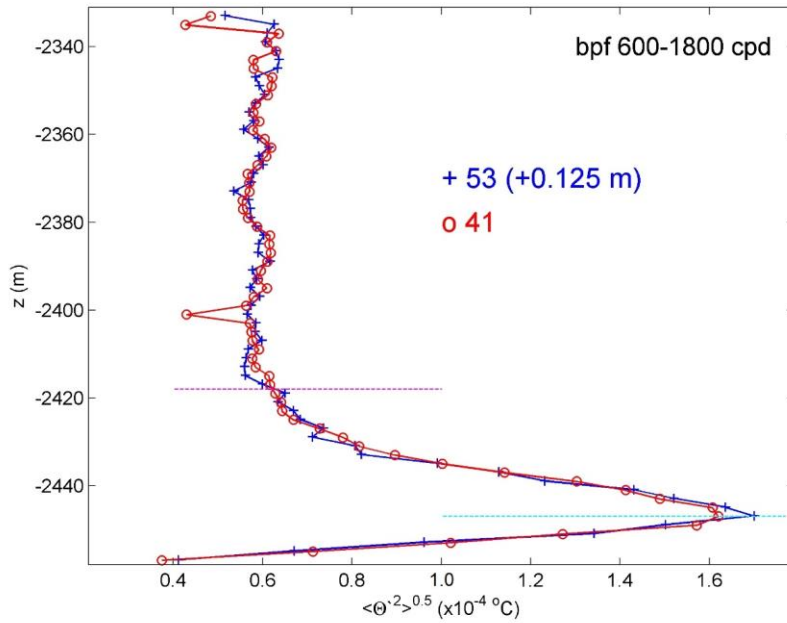
485
 486 **Figure 6.** Vertical displacement calculation for vertical lines of the large-ring mooring using the local
 487 adiabatic lapse rate Γ . This height-determination method is based on temperature shift per line after
 488 calibration and drift correction for near-homogeneous period 350.04-350.08, with arbitrary line 53 as
 489 reference. The conversion of meters into degrees Celsius is via $\Gamma = 0.00017^{\circ}\text{C m}^{-1}$, so that a vertical
 490 difference of $dz = 3$ m reflects approximately 0.0005°C . Corner-lines are 17, 18, 26, 38, 47, 48, 62 and
 491 66.



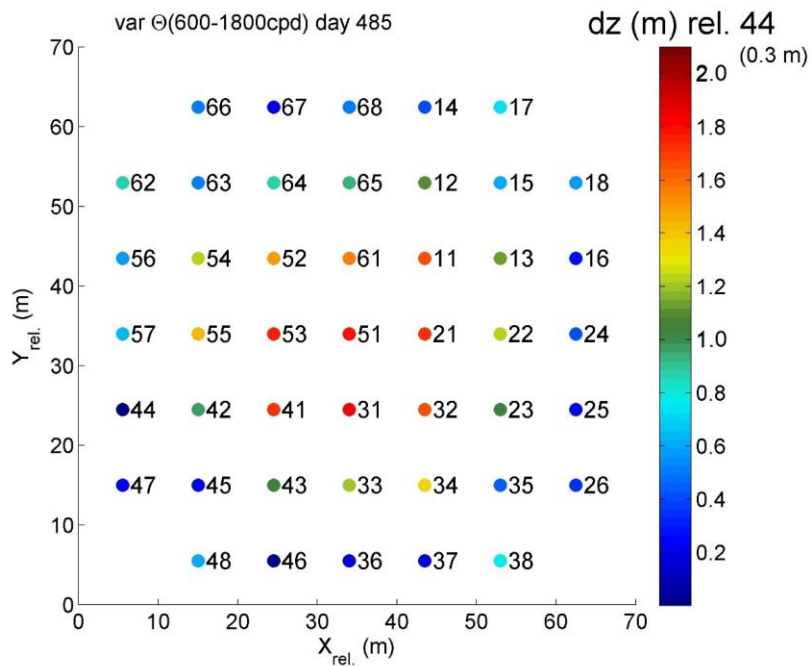
492
 493 **Figure 7.** Thirty-one hours of data from line 53 during a turbulent passage of relatively warm water.
 494 Horizontal dashed magenta and cyan reference lines are at $h = 40$ and 11 m above seafloor, respectively.
 495 (a) Time-depth plot of Conservative Temperature with black-dotted contours every 0.001°C . low-pass
 496 filtered ‘lpf’ with cut-off at 3000 cpd (cycles per day). (b) Logarithm of 2-m small-scale buoyancy
 497 frequency from reordered profiles of data in a. (c) Logarithm of non-averaged displacement values from
 498 data in a. following the reordering method by Thorpe (1977) and cast in units of turbulence dissipation
 499 rate. (d) Time series of logarithm of turbulence dissipation rate averaged over the 124-m vertical extent
 500 of T-sensors.
 501



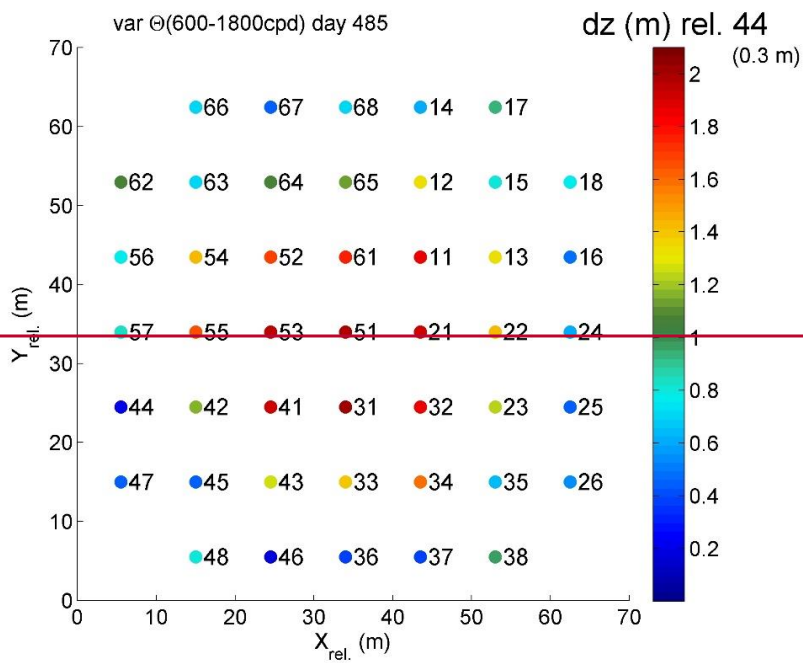
502
 503 **Figure 8.** Unscaled frequency spectra, patched from weakly and heavily smoothed parts, for four T-
 504 sensors of line 53 at indicated heights h above seafloor, averaged over the 1.3-day period of Fig. 7 for
 505 unfiltered data. Spectral slopes ω^p for inertial and buoyancy subranges of turbulence are indicated with
 506 straight dashed lines and exponents p . The horizontal black bar indicates frequency range of the pass-
 507 filter band that is applied for the turbulence-variance method of height determination.
 508



509
 510 **Figure 9.** Vertical profiles of standard deviation of band-pass filtered ‘bpf’ high-frequency turbulence
 511 signals for temperature data in Figs 7a, 8 for two neighbouring lines, with off-set relative height
 512 determination. The variance-peak height (cyan-dashed line) corresponds also to the height of strongest
 513 layering in stratification in Fig. 7b. The magenta-dashed line delineates the vertical extent of enhanced
 514 temperature variance above interior values.
 515

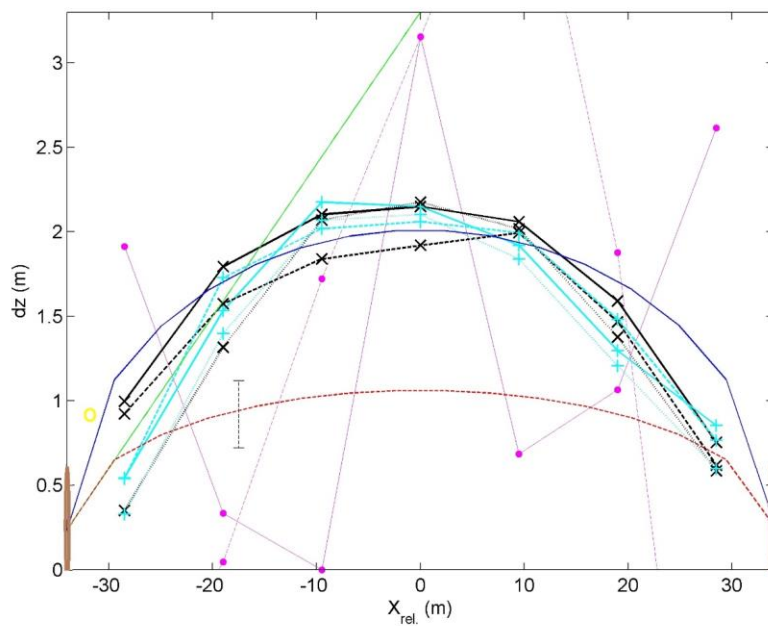


516

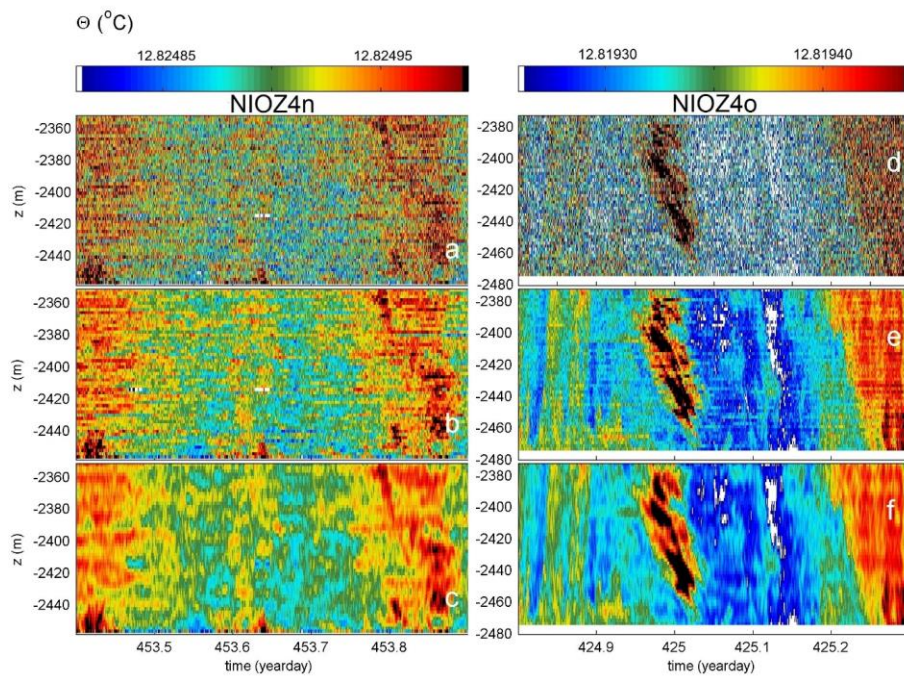


517

518 **Figure 10.** As Fig. 6, but for turbulence-variance height-determination method determined from profiles
 519 like in Fig. 9 using T-sensor data between positions 2 and 3 above seafloor, where the gradient in
 520 temperature variance is maximum, divided by the average gradient over 2 m. Values are given relative
 521 to those of line 44 (0.3 m), arbitrary line near the edge of the cable-grid.
 522

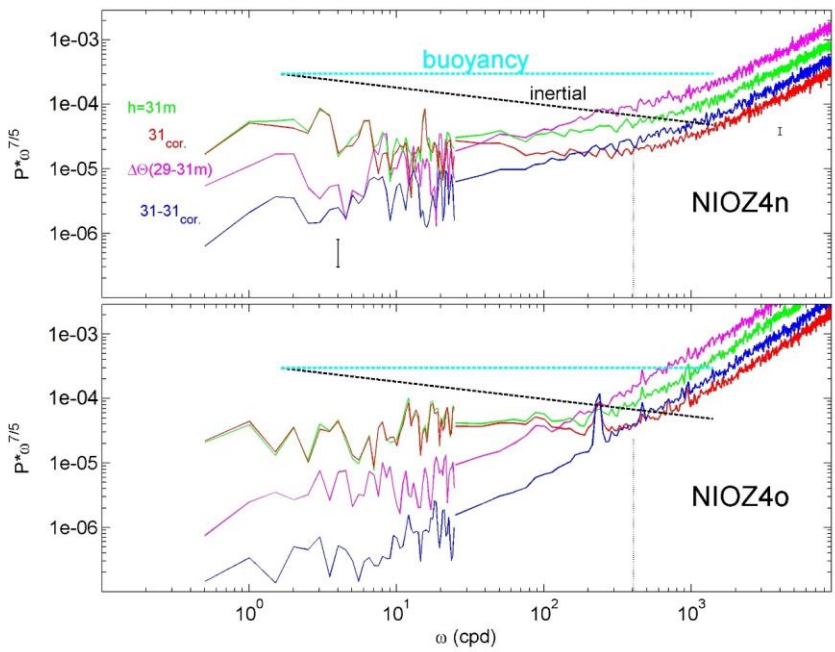


523
 524 **Figure 11.** Constant-Y (black x graphs) and constant-X (cyan +) cross-sections without corner-lines of
 525 height determinations from Fig. 10 vertically shifted +0.3 m. Solid lines indicate center lines in both
 526 directions. Corner-line height determination is indicated by yellow o. For comparison, data in Fig. 6 are
 527 given for central lines with magenta dots (thin solid x-direction; dashed y-direction). In the background,
 528 models are given in green, blue and red of double distance than in Fig. 3.
 529

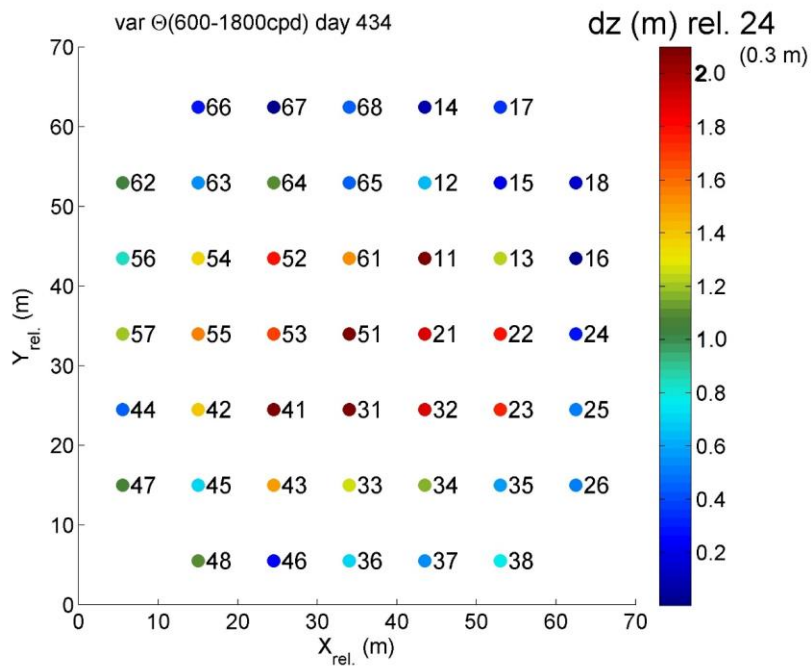


530
 531 **Figure A1.** Half-day Conservative-Temperature data from $h = 1-104$ m demonstrating the correction of
 532 short-term drift. The conditions are near homogeneous, as full the temperature range is only 1.7×10^{-4} °C
 533 during both the present experiment in 2020/2021 (left column) and during a test-experiment in 22-m
 534 deeper water in 2017/2018 (right column). (a, d). Unfiltered data, after post-processing involving
 535 calibration, referencing to CTD-, homogeneous-period-, and smooth-polynomial data. (b, e) ~~Lpf~~ low-pass
 536 ~~filtered lpf~~ filtered lpf with cut-off at 500 cpd. (c, f) Corrected for short-term drift: 500-cpd and 10-m vertical-
 537 scale lpf data.

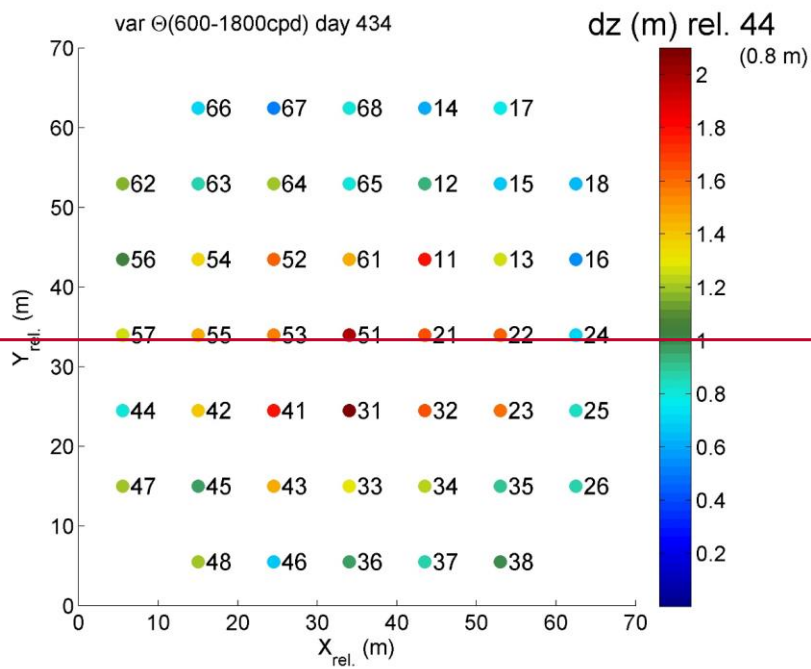
538



539
 540 **Figure A2.** Four-day average spectra that are patched together from two, a weakly- and a heavily
 541 smoothed part, and scaled with the buoyancy-subrange slope (horizontal cyan). [From 2-s sampled T-](#)
 542 [sensor data.](#) The spectra demonstrate effects of and correction for short-term drift in T-sensor data
 543 around $h = 30$ m during near-homogeneous periods between days 453-457, including those of Fig. A1.
 544 Plotted are spectra for unfiltered data (green), vertical temperature difference with data from T-sensor
 545 2-m lower (magenta), 500-cpd and 10-m vertical scale corrected data (red), and the difference between
 546 green and red spectra (blue). For reference, the relative log-log plot slope is given for inertial subrange
 547 (black). The vertical dotted line at 400 cpd is explained in the text. a) NIOZ4n data. b) NIOZ4o data.
 548



549



550

551 **Figure A3.** As Fig. 10, but for a 3.6 h short warm-water period between days 434.95 and 435.1 and
552 relative to line 24. The temperature variance gradient is determined between positions 2 and 4 (dz = 4
553 m) above seafloor for some smoothing.

554